

SN Computer Science

Spatially Adapted Statistical Segmentation I Reversing distortive X-ray effects for Accurate Implant-contact Tissue Classification in Bone SR μ CT

--Manuscript Draft--

Manuscript Number:	SNCS-D-23-00204	
Full Title:	Spatially Adapted Statistical Segmentation I Reversing distortive X-ray effects for Accurate Implant-contact Tissue Classification in Bone SR μ CT	
Article Type:	Original Research	
Section/Category:	Other	
Funding Information:	Villum Fonden (41017)	Prof James Avery
	HORIZON EUROPE European Research Council (779322)	Prof Else Marie Pinholt
	Innovationsfonden (8057-00012B)	Dr Carl-Johannes Johnsen
Abstract:	<p>Synchrotron Radiation micro-CT (SRμCT) produces 3D images at extremely high fidelity. However, while distortive X-ray effects such as beam-hardening are minimized due to highly brilliant monochromatic beams, they are not eliminated. In particular, obtaining accurate tissue classification is a challenge near high-contrast interfaces such as metal implants. We present a computational method that discovers the image distortion as a function of space, and produces continuous probabilistic models of material classification functions. Using the derived models, we are able to accurately classify tissue throughout the full image, even at high-contrast transition interfaces. We apply the method to solve the notoriously difficult problem of accurately classifying biological tissue in contact with a titanium implant. The new tissue classification method was used to evaluate bone-to-implant contact (BIC) in micrometer-resolution SRμCT images. In a previous study, we were unable to obtain accurate results for BIC, due to difficulties in accurately classifying the tissue types near the titanium implant surface. In the present work, we invert the distortive effects and obtain accurate tissue classification all the way to the implant surface. The method is implemented in C++ and Python, and is parallelized for GPU and multi-core CPU. To deal with the very large 3D image sizes arising from SRμCT, exceeding system memory on even large workstations, the algorithms are designed to run out-of-core on multi-resolution representations of the tomograms.</p>	
Corresponding Author:	James Avery, Ph.D. University of Copenhagen Copenhagen, DENMARK	
Corresponding Author Secondary Information:		
Corresponding Author's Institution:	University of Copenhagen	
Corresponding Author's Secondary Institution:		
First Author:	James Avery, Ph.D.	
First Author Secondary Information:		
Order of Authors:	James Avery, Ph.D. Aleksandar Topic Carl-Johannes Johnsen, PhD Else Marie Pinholt, Dr. Odont	
Order of Authors Secondary Information:		
Author Comments:		

Suggested Reviewers:	Jean Michelle Létang, PhD Researcher, CREATIS: Centre de Recherche en Acquisition et Traitement de l'Image pour la Santé letang@creatis.insa-lyon.fr Prof. Letang is an expert in medical CT imaging techniques.
	Frank P. Vidal, PhD Senior Lecturer, Bangor University f.vidal@bangor.ac.uk Prof. Vidal is an expert on medical simulation software and X-ray imaging.

[Click here to view linked References](#)

10

11

12

13

14

15

16

17

18

19

Spatially Adapted Statistical Segmentation I: Reversing distortive X-ray effects for Accurate Implant-contact Tissue Classification in Bone SR μ CT

20

21

22

23

24

25

26

27

28

29

30

James Avery^{1,2,3*}, Aleksandar Topic¹, Carl-Johannes
Johnsen^{1,2} and Else Pinholt⁴

31

32

33

34

35

36

37

38

39

40

41

42

43

44

45

46

47

48

49

Abstract

50

51

52

53

54

55

56

57

58

59

60

61

62

63

64

65

2 Spatially Adapted Statistical Segmentation

the method to solve the notoriously difficult problem of accurately classifying biological tissue in contact with a titanium implant. The new tissue classification method was used to evaluate bone-to-implant contact (BIC) in micrometer-resolution SR μ CT images. In a previous study, we were unable to obtain accurate results for BIC, due to difficulties in accurately classifying the tissue types near the titanium implant surface. In the present work, we invert the distortive effects and obtain accurate tissue classification all the way to the implant surface. The method is implemented in C++ and Python, and is parallelized for GPU and multi-core CPU. To deal with the very large 3D image sizes arising from SR μ CT, exceeding system memory on even large workstations, the algorithms are designed to run out-of-core on multi-resolution representations of the tomograms.

Keywords: Image analysis, Tissue classification, Osseointegration, Segmentation, Bone-to-implant contact, Synchrotron Radiation micro-CT

MSC Classification: 92C55 , 62H35

1 Introduction

1.1 Image data

Bone samples are most commonly analysed by extracting histologies and examining their two-dimensional structure with light microscopy. This method has several drawbacks. First and foremost, it is destructive: In addition to the obvious issue that the histology must be cut from the full sample, the sawing process can contaminate soft tissue with bone dust, or leave surface scratches that complicate automatic image analysis. Secondly, histology by its nature only gives a two-dimensional slice of the full three-dimensional picture. Most important biological structures are inherently three-dimensional, and limiting analysis to 2D severely restricts the types of questions we can answer.

Synchrotron Radiation micro-tomography (SR μ CT) offers a non-destructive high-quality alternative to histology for detailed analysis of bone biopsies. [1] quantified the uncertainty of 2D histology for four common bone analyses, and found that the choice of sampling plane for histological analysis incurred a significant uncertainty in the results, whereas the full volumetric analysis of SR μ CT tomograms did not.

The high brilliance and collimation of synchrotron radiation yields particularly faithful 3D images, as common distortive X-ray effects seen in hospital-grade setups such as beam hardening and projection artefacts are minimized. The high fidelity makes SR μ CT attractive for conducting advanced medical image analyses with trustworthy results.

However, while image distortion effects are much reduced compared to laboratory X-ray tomography, they are not eliminated, and numerical analysis and computations on the images must still be conducted carefully. Boundary

21 effects near sample surfaces, ring artefacts from sensor faults, and especially
22 distortion near high-contrast transitions, make accurate tissue classification
23 difficult in regions where this distortion is significant. [2] found that, while they
24 could accurately classify bone tissue in the middle regions of the tomograms,
25 they were not able to obtain good bone-to-implant contact evaluation (BIC),
26 as evidenced by poor correlation with histological analysis of the same samples.
27

28 The present work presents a fully automatic computational method which
29 discovers probabilistic models for the distortions incurred by the physical
30 effects in high-resolution X-ray CT such as SR μ CT in order to reverse them
31 and produce accurate tissue classification even in regions where these effects
32 are significant. It exploits two properties, which are needed to hold for the
33 method to work: i) very high resolution is used to build statistical models as
34 functions of space, and ii) the effects to be countered must vary continuously
35 over space, so that we can track how voxel frequency distributions are dis-
36 torted throughout the image. We apply the method to the same dataset of
37 micrometer-resolution SR μ CT bone tomograms studied in [1] and in [2], to
38 achieve faithful tissue classification all the way to the titanium implant surface.
39

40 Our goal is to obtain good conditional probability distributions $P(m|v|\mathbf{x})$
41 that model the likelihood of a voxel having material type m as a function
42 both on its value v and its position \mathbf{x} in the tomogram. We want to make sure
43 that these distribution functions vary smoothly across space, to ensure that we
44 can identify the materials correctly across the entire image: even though the
45 frequency distributions look completely different close to the titanium implant
46 compared to the middle region or sample surface, we can track the unbroken,
47 smooth deformation to assign a global material identity.
48

49 The aims of the current work is:
50

- 51 1. To design a fully automatic **spatially aware segmentation algorithm**
52 that improves segmentation quality of tissues in bone-SR μ CT in all regions,
53 including near high-contrast interfaces.
- 54 2. To implement this method efficiently in open-source software for GPU and
55 multi-core CPU using out-of-core techniques, to facilitate analysis of 3D
56 SR μ CT images that exceed system memory.
- 57 3. To use the new method to evaluate bone-to-implant contact closer to
58 implant surfaces than previously feasible.

59 2 Background

60 The methods presented in this paper were devised as part of development
61 of a larger software toolbox for fully automatic analysis of very-high resolu-
62 tion SR μ CT bone tomograms. Presently, the work is focused on automatic
63 analysis of an experiment conducted to evaluate four different methodologies
64 for stimulating bone regeneration in goat mandibles, described below. The
65 software system is also being developed as preparatory work for analysis of
SR μ CT bone tomograms from 150 human patients in the MAXIBONE project
(www.maxibone.eu). This project aims to create personalized maxillary bone

4 Spatially Adapted Statistical Segmentation

regeneration by using culture expanded autologous bone marrow stem cells and biomaterials, for which clinical trials are presently being conducted. The data set used in the present work is 35 high-resolution tomograms of old and regenerated goat mandible bone samples, in order to evaluate the amount and health of regenerated bone, and in particular zooming in on osseointegration against the titanium implants closer than was previously done.

2.1 Background for the medical experiment

Installation of a dental implant initiates the Regional Acceleratory Phenomenon (RAP), which implies acceleration of the different healing stages. RAP begins a few days after implant installation, peaks at 1-2 months, and subsides after 6-24 months [3]. In cortical bone, the non-vital mineralized tissue initially needs to be resorbed prior to bone formation. In the cancellous compartment, the implant installation mainly results in damage of marrow spaces with resulting local bleeding and coagulum formation. The coagulum gradually resorbs, collagen is laid down and replaced by osteoid, and eventually — if sufficient blood supply is present — woven immature bone develops, and sequentially osseointegration is initiated [3]. After 6-12 weeks of healing most of the woven bone is mineralized and bone marrow containing blood vessels, adipocytes, and mesenchymal cells can be observed surrounding the trabeculae in the mineralized bone [4, 5]. A cement line, thickness 0.2-5 µm, will be deposited directly on the implant surface during continuous bone formation. The biological fixation of the implant initiates only a few days after implant installation, where the osteoblasts begin to deposit collagen matrix on the cement line. This early deposition of calcified matrix followed by the arrangement of woven bone and later mature cancellous bone develops in a 3D manner delimiting the marrow space [6].

2.2 Physical samples

The experiment evaluated four methods for stimulating maxillary bone regeneration. 5 critical size defects were introduced to 7 goats. Four defects were used to asses bone regeneration methods, and one was a control sample. Peri-implant vertical bone augmentation was performed using autologous bone and two different calcium phosphate bone substitutes. The bone specimens were evaluated undecalcified. The specimen preparation was performed at the Department of Biomaterials at Gothenburg University, Sweden. The specimens were initially fixated in 4% paraformaldehyde. Dehydration of the specimens was performed in increasing concentrations of ethanol to eliminate fat and water content. Furthermore, specimens were infiltrated with methylmethacrylate (MMA) and embedded in molds 12 mm in diameter and 20 mm in height [7]. They were scanned at the European Synchrotron Radiation Facility (ESRF) in Grenoble, France. The advantage of using MMA is greater tissue penetration than water-soluble methacrylates. This is an advantage when preparing larger specimens such as bone biopsies containing dental

implants. Furthermore, the histological quality of bone sections is generally higher for MMA embedded specimens compared to water-soluble methacrylates [8]. Additionally, tissue shrinkage is less than 2% when using MMA embedded bone and cartilage specimens [9].

Physical samples were prepared for SR μ CT scanning by cutting out portions from the larger cylindrical biopsies. Within these samples, we find the titanium dental implant (Astra Tech OsseoSpeed, ST Molndal, Sweden). It is 3.5mm in diameter and 8mm long. Along its length the lower 5.5mm has larger threads and is attached to recipient bone. The upper 2.5mm has smaller threads and is where newly formed bone is to be assessed. Surrounding the bone and implant contact-region are cavities containing resin, air, blood vessels and other fibrous tissue.

A cut sample is shown in three different cross sectional views in Figure 1. Each material has a unique density and thus absorption. The titanium implant shown in blue has a higher absorption level than bone. Bone material shown in light orange has higher absorption than its surrounding dark orange colored regions containing blood vessels tissue, air and resin.

32 33 34 35 36 37 38 39 40 41 42 43 44 45 46 47 48 49 50 51 52 53 54 55 56 57 58 59 60 61 62 63 64 65 **2.2.1 Data acquisition**

It can be difficult to study and evaluate the bone structure and blood network without destroying or manipulating the sample. X-ray computed tomography is a widely used tool for non-intrusive medical imaging. By exposing a subject to X-rays, we can map the linear attenuation coefficient of the passing rays. Each ray is attenuated relatively to the density and composition of the material it passes. By rotating either the scanner or the sample we can get a full 3D image representation of the inner structure of the sample. Each volumetric pixel (voxel) then represents the X-ray attenuation at its spatial position. In this way, X-rays can reliably be used to internally characterise samples in a non-intrusive and non-destructive manner. Medical CT-scans can provide spatial resolutions on the order of submillimetre scale [10]. The more modern micro computed tomography (μ CT) can provide much higher spatial resolution on the micrometre scale [11].

This work focuses on a data set acquired by Synchrotron Radiation micro-CT (SR μ CT). For this imaging technique, electrons are accelerated to ultra-relativistic speeds in trajectories directed by strong magnetic fields. The resulting X-ray beam provides a high photon flux allowing for very short exposure times [11]. This can help counter Poisson noise from suboptimal photon count [12]. Contrary to both CT and μ CT, this approach requires a large particle accelerator, and is not standard medical or laboratory equipment. However, SR μ CT offers an even better spatial resolution of up to 0.1 μ m, and much higher image quality due to fewer distortive X-ray effects. The resulting beams are high in brilliance and collimation, which gives a very clear signal. Artifacts from beam-hardening are minimized due to synchrotron radiation X-rays being characterized by their practically mono-energetic spectrum.

6 Spatially Adapted Statistical Segmentation

The tomograms presented here have been acquired at the ID19 beam line at the European Synchrotron Radiation Facility (ESRF) in Grenoble, France. They were reconstructed[2] at the ID19 beamline. A standard filtered back-projection algorithm was applied via the ESRF in-house developed software PyHST [7, 13]. PyHST was applied to improve reconstruction quality, hence reducing ring artefacts, and to reduce the required data volume if necessary [14]. The tomograms were acquired at 50 KeV.

2.2.2 Image data

The physical field-of-view of a single image sample is about 6.5mm in each direction. Each sample contains voxels with a spatial resolution of $1.875\mu\text{m}$. The samples are scanned in chunks of 4-6 sub-volumes through the height of the implant, depending on the initial size of a sample.

As the scans slightly overlap, we first compute the overlaps between volumes, by shifting along the Z-axis until the square 3D image differences are minimized over the overlap volume, producing the best volume match. This allows us to combine the sub-volumes into a single coherent 3D image of the full sample. The images are represented in a custom hierarchical image format to facilitate fast multiresolution analysis. The full image has resolution (3456, 3456, 3360) (ensured to be divisible by $32 = 2^5$), and has 5 coarse layers at resolution divided by 2, 4, 8, 16, and 32.

3 Physical effects

Noise in tomography is unavoidable, and it makes segmentation harder because it further obscures the boundaries between materials. Materials may be well separated from certain angles in the 3d-reconstructed image, but can overlap from others. Some noise like that corrected by flat-field correction is very uniformly distributed across images. Other noise is however very spatially dependent on its surrounding regions. Knowing the composition and positioning of the materials being imaged, we can counter some of these effects during segmentation. The effects from noise manifest themselves as numerical shifts in voxel-values as a function of their position. This is a direct result of a misrepresented attenuation along the axis the X-rays are passing.

This dependency on orientation illustrates how voxel intensity values are not globally fixed. Instead, how a certain material is represented in intensity, is highly dependent on its position relative to neighbouring regions. Especially since this also determines the amount and type of derived noise. The same material with the same density, can thus be represented at multiple varying intensities within the same sample.

In Figure 2, we see zoomed in regions of the XY- and YZ-planes of the same sample as shown in Figure 1. Both planes display a broad selection of the various type of noise sources found in the data.

- **Beam hardening:** Medical CT and μ CT both utilize poly-energetic beams, which can cause artefacts around high density regions. This effect is called

beam-hardening [15], and occurs when rays with lower energy are attenuated more frequently, thus shifting the remaining photon energy to a higher effective average value. This offsets the local contrast, by overestimating the attenuation, leaving lighter spots on the image. Many types of artefacts will typically be present in X-ray setups, but most are taken into account by calibration using phantoms and pre-hardening the beam before it reaches the sample. Pre-hardening of the beam is done using filters that attenuate the softest rays. Due to its common usage, various metal artefact reduction (MAR) software exists to account for noise and imperfections during reconstruction [16][17].

Despite the practically mono-energetic rays from SR μ CT, the source initially generates a poly-chromatic spectrum. During monochromatisation the resulting spectrum can still contain corrupted harmonic components. Only a few percent corruption is enough to produce strong artefacts, although monochromatisation is typically done in multiple layers [12]. It can not trivially be rejected that some noise does occur from poly-energetic incident radiation. Two distinct effects typically seen as a result of beam-hardening are in dark and bright streaks and cupping artefacts in high density regions.

- **Dark and bright streaks:** Streaking artefacts occur at the dense implant region, but also in the transition from bone to softer tissue. This effect is mostly seen in regions of large heterogeneity. When X-ray beams pass at angles containing multiple dense obstacles, the beam is hardened more. Then for angles with fewer dense obstacles the energy spectrum is preserved better. This produced the dark and bright streaks seen in Figure 2. For a hardened beam, softer x-rays are absorbed instead of successfully penetrating the object, and will not contribute to image formation. High density structures such as the titanium implant break the isotropy, making the projected X-ray mean energy spectrum dependent on incident orientation [12].
- **Cupping effect:** A common artefact that occurs when beams pass more homogeneous cylindrical objects. Since beams passing the middle will traverse more material compared to the edges, the beam is hardened more towards the center and intensity becomes lower as a result. This can manifest itself in what erroneously looks to be dense peripheral regions at the edges.
- **Phase contrast:** Phase contrast is an effect whose consequences are not very unlike those of beam-hardening. Although used as an advantage in holotomography[18] and phase contrast tomography[19], it induces noise in regular tomography such as used here. It typically results in fringes around edges of regions within the image[12]. Similar to dark and bright streaks mentioned above, they show as misrepresentations of the voxel values. In our case we see them especially at the transitional edges between the titanium implant and the biological tissue and bone.
- **Ring artefacts:** Looking at the XY-plane in Figure 2(a) we see clear concentric ring artefacts emanating from the center of the sample, and at strong edges of the titanium implant. It propagates strongly through the large

8 Spatially Adapted Statistical Segmentation

region of air behind the implant. Compared to the other artefacts mentioned, this effect is arising from imperfections in the scanner setup. These types of artefacts can typically come from uncalibrated or defect adjacent detector elements. For synchrotron radiation sources it can also occur from shifts and vibrations in the monochromator crystal [20].

- **Projection artefacts:** Bright streaks with strong edges are seen from the sharp corners of the titanium implant. When doing back projection, a symmetry break is seen as smeared lines across the sample. This can occur from the high pass filter used during filtered back projection, which exaggerates the differences between adjacent elements [21].
- **Compton scattering:** Lower energy rays contribute mostly with noise from scattering effects. A ray will propagate through a material, get scattered and diffract from its initial trajectory. This gives a misrepresentation of the attenuation along its initial trajectory. The artefacts seen from scattering are similar in nature to those formed by beam hardening. This is because both phenomena effectively reduce the measured attenuation. For energy levels relevant for the data presented here, of 50 KeV and above, Compton scattering is the dominant type [22]. The scattering occurs due to photon-electron interaction between X-ray beam and the material it passes through. Like beam-hardening, scattering will cause dark streaks across the image, where attenuation was highest.

The distortions that come from the class of physical effects and noise artefacts discussed in this section, will vary continuously as a function of the spatial coordinates. This allows the possibility for a method, which can correctly identify materials despite varying voxel values.

4 Method

In this section, we will describe the method for exploiting spatial correlation based on the 2D-histograms of the tomographies. We will start by motivating the problem, then give an overview of how we solve the problem, with a final detailed walk-through of each step in the overall workflow.

4.1 1-dimensional histograms

Looking at a 1D-histogram of the voxel value in a tomography, as shown in [Figure 3](#), we are able to distinguish different distributions, but we see that there are large overlaps. This leads to global thresholding being infeasible, at least for the distributions in the lower half of the histogram. This happens because the voxel value is not globally defined, as [Section 3](#) explains, which illustrates how the different materials cover ranges of values that blend together in the histogram.

4.2 Preprocessing

To reduce the complexity of the segmentation process, we preprocess the data by removing redundant information. We first compute a coarse bone-region using a crude segmentation. Through a direct geometric analysis of the implant, we determine the sample coordinate system, with the origin on the back-plane of the sawed-through implants and principal axes coordinate system vectors \mathbf{u} pointing up towards the implant top, \mathbf{v} pointing forward away from the back-plane, and \mathbf{w} point right, parallel to the back-plane. An automatic wave-analysis of the threads computationally determines the macro-threaded recipient bone region, and the micro-threaded de-novo regenerated bone region. We then perform the spatially-aware segmentation analysis restricted to the bone-regions in order to not expand effort on the parts of the segmentation problem that can be solved with simpler methods. Note that the process is fully automatic, and does not require human intervention.

4.3 Exploiting spatial information

Our goal is to discover how the value distributions for the different materials – bone, blood vessels, etc. – change as a function of space. In other words, we wish to uncover information about the conditional probabilities $P(m|v, \mathbf{x})$: that a voxel with value v and position \mathbf{x} represents material m . We cannot compute this directly using only the image, as only one voxel occupies position \mathbf{x} .

However, if we fix one axis x , y , or z , the image *does* contain millions of voxels with that fixed value, enough to make good statistical models for e.g. the conditional probabilities $P(m|v, x)$, $P(m|v, y)$, and $P(m|v, z)$. To this end, we compute 2D histograms that count voxel frequencies both conditioned on value v and coordinate value along either x , y , or z .

Figure 4(a) shows the histogram for our model tomogram (implant excluded) as a function of the y coordinate: each row in the image is a histogram for a fixed value of y . Figure 1(a) helps us see what happens: For $y < 2400\mu\text{m}$, there is only air, then we reach a thin layer of resin, after which we enter the region where we find bone, soft tissue, resin, and air. The air voxels are brightened as we approach the implant, shifting the peaks smoothly rightwards. A better coordinate system for capturing both the distortive edge-effects, and the glow from the implant, is to use cylindrical coordinates with respect to the implant center line. This is computed automatically as the centers for the least-squares optimal circles with respect to the implant along the principal axis. Figure 4(b) shows a similar 2D histogram for the radial cylinder coordinate $r = \sqrt{(x - c_x(z))^2 + (y - c_y(z))^2}$. From this plot, we see two prominent distributions that change along the r axis. The radius correlates with distance to the sample surface (capturing edge effects), and for medium r , it is a good proxy for distance to the implant, and we see a brightening with smaller r , and a darkening and broadening of the distributions for large r . Each

10 *Spatially Adapted Statistical Segmentation*

view provides us with additional information about how voxel values are distorted throughout space: analogous to casting shadows along different axes to obtain more information about a 3D object. We can either use Bayesian statistics to combine information from multiple axes, or construct a spatial grouping that is particularly suited to capture the effects of the distortive effects that we want to counter. The next section describes the latter.

4.4 Field histograms

In the present work, the main distortion that we want to invert is the brightening of voxels near the high-contrast interface between titanium implant and biological tissue, in order to accurately determine tissue-implant contact. To this end, we can group the voxels according to their distance to the implant using the *Euclidean Distance Transform* (EDT). Figure 4(c) shows the corresponding 2D histogram, which shows a darkening effect for large distances (near the sample surface) and brightening for small distances (near the implant surface).

However, we can do better: As discussed in Section 3, the implant produces a *glowing* effect, which can be modeled physically by diffusion. Figure 5 shows how a voxel inside the troughs of the threading receives brightening contributions from many sides, while a voxel above the peak of the threading at the same distance from the implant receives much less. To resolve brightening of voxels very close to the implant, it thus makes sense to use a diffusion field, as shown in Figure 6.

By using a diffusion field to model the glow from the implant, we are able to describe the brightening effect even very close to the implant, but the field is nearly zero everywhere else. In order to construct a single field that separates voxels well according to the major contributions of distortion, we construct a combined EDT+diffusion field. We will see in the next section that this is enough to produce a high-quality segmentation throughout the tomogram, both near the implant surface and far away from it.

4.5 Walk-through of the method

This section will describe each step of our method in detail. Going from tomography to a segmented tomography.

4.5.1 Overview

In order to reach the tissue-bone implant contact metric, we have the three coarse steps: compute the fields, segmentation using the fields, and extraction of the contact from the segmented tomography. The steps of the field computation are:

1. Compute the EDT and Diffusion fields to give each voxel spatial information about its relation to the implant.

- 14 2. Compute frequency distributions of voxel values as functions of field values
 15 as 2D histograms.

16 Then, in order to segment using the fields:

- 17 3 Find the material ridges within the 2D histograms, using image processing
 18 techniques.
 19 4 From the ridges, compute initial approximate frequency distributions of
 20 each material, which are then optimized to fit the 2D histograms. From
 21 the optimized distributions, we derive probability distributions for material
 22 classification. These distributions approximate the conditional probabilities
 23 $P(m|v, x)$ that a particular voxel belongs to material m given that it has
 24 voxel value v and field value x .
 25 5 Apply the probability distributions to the tomography, segmenting the
 26 voxels into the different materials.

27 In the present paper, we use the improved segmentation to evaluate bone-
 28 implant contact and blood-implant contact.

- 29 6 From the segmented tomography, we compute the network of blood vessels
 30 and the osteocyte network. Voxels are classified as bone, if they are in a
 31 connected component of bone-mineral and within a maximal distance from
 32 blood supply and osteocytes.
 33 7 Perform the tissue-to-implant contact analysis.

34 These steps are also summarized in the flow chart in [Figure 7](#).

40 4.5.2 Segmentation

41 The overall segmentation is computed in steps 1-5. For each step we will
 42 describe the process, showing the algorithm where applicable, along with the
 43 the intermediate results.

45 *Step 1: Field computations*

46 Both fields are computed from the implant mask, as described in [Section 4.2](#).
 47 EDT is computed in parallel using W. Silversmith's implementation of Mei-
 48 jister's algorithm [23], yielding a 3D image in which every non-implant voxel is
 49 the Euclidean distance to the nearest implant voxel.
 50

51 For diffusion, rather than solving a full diffusion equation, we approxi-
 52 mate it using repeated convolutions of a 3D-Gaussian kernel, implemented by
 53 separating into 1D convolutions, as seen in [Algorithm 1](#), and the XZ-plane
 54 in [Figure 6](#).

55 To obtain a good separation both close to the implant and far away, we
 56 combine the two fields into a single one as shown in [Equation \(1\)](#).

$$57 \\ 58 \\ 59 f_{combined} = \frac{f_{diffusion} - \frac{f_{edt}}{\max(f_{edt})} \min(f_{diffusion})}{\max(f_{diffusion})} \quad (1) \\ 60 \\ 61 \\ 62 \\ 63 \\ 64 \\ 65$$

12 *Spatially Adapted Statistical Segmentation***Algorithm 1** Diffusion approximation.

```

15   function DIFFUSION(voxels[ $n_z * n_y * n_x$ ],  $n_{\text{repetitions}}$ ,
16     kernel[ $2 * k + 1$ ])
17      $S \leftarrow [n_y * n_x, n_x, 1]$ 
18      $N \leftarrow [n_z, n_y, n_x]$ 
19     buf0[:]  $\leftarrow$  voxels[:,]
20     for rep in 0: $n_{\text{repetitions}}$  do
21       for dim in 0:3 do
22         for  $z, y, x$  in 0: $n_z, 0:n_y, 0:n_x$  do
23            $X \leftarrow [z, y, x]$ 
24            $i_{\text{start}} \leftarrow -\min(k, X[\text{dim}])$ 
25            $i_{\text{end}} \leftarrow \min(k, N[\text{dim}] - X[\text{dim}] - 1)$ 
26            $i_{\text{global}} \leftarrow z * S[0] + y * S[1] + x * S[2]$ 
27           for i in  $i_{\text{start}} : i_{\text{end}}$  do
28              $i_{\text{offset}} \leftarrow i_{\text{global}} + i * S[\text{dim}]$ 
29             buf1[ $i_{\text{global}}$ ]  $\leftarrow$  buf0[ $i_{\text{offset}}$ ] * kernel[i + k]
30             end for
31           buf0[:]  $\leftarrow$  buf1[:]
32         end for
33       end for
34     end for
35   end function

```

Step 2: 2D histograms

From the combined fields we compute a 2D-histogram with the field value on the y-axis and the voxel value on the x-axis. The algorithm for the field-histogram can be seen in [Algorithm 2](#) along with a plot of the resulting histogram in [Figure 8](#). We see that the bone and soft tissue separate neatly into two distinguishable distributions. The effect of the diffusion field is to “zoom in” near the implant surface, where the diffusion field changes rapidly.

Step 3: Identify the materials

In order to decompose 2D histogram into a sum of probability distributions that represent the different materials present in the tomogram, we first identify the *ridges*: i.e., the peaks in the 1D histograms that are persistent and vary continuously with the field value. Thus we can expect each ridge to represent the *expectation values* for a particular material as a function of the field value, i.e., as a function of the voxel’s position in space. Any ridge-finding method will do: we compute it through the series of image processing operations shown in [Algorithm 3](#).

Step 4: Compute models for material probability distributions

Our goal is to obtain good conditional probability distributions $P(m|v, \mathbf{x})$ that model the likelihood of a voxel having material type m as a function both on

10

11

12

13

14

15

16

17

18

19

20

21

22

23

24

25

26

27

28

29

30

31

32

33

34

35

36

37

38

39

40

41

42

43

44

45

46

47

48

49

50

51

52

53

54

55

56

57

58

59

60

61

62

63

64

65

Algorithm 2 Field 2D histograms.

```

function FIELD_HIST(voxels[nz, ny, nx], field[nz, ny, nx], vbins, vmin, vmax,
fbins, fmin, fmax)
    for z, y, x in 0:nz, 0:ny, 0:nx do
        v  $\leftarrow$  voxels[z, y, x]
        if vmin  $\leq$  v  $\leq$  vmax then
            f  $\leftarrow$  field[z, y, x]
            if fmin  $\leq$  f  $\leq$  fmax then
                vi  $\leftarrow$  (vbins - 1) -  $\frac{v - v_{\min}}{v_{\max} - v_{\min}}$ 
                fi  $\leftarrow$  (fbins - 1) -  $\frac{f - f_{\min}}{f_{\max} - f_{\min}}$ 
                h[fi, vi]++
            end if
        end if
    end for
    return h
end function

```

Algorithm 3 2D histogram ridge-finding.

```

function RIDGES(h[fbins, vbins], σ, peakmin, kx, ky,
idilate, ierode, t)
    for row in 0:fbins do
        r  $\leftarrow$  gaussian_smooth(h[row, :], σ)
        p  $\leftarrow$  find_peaks(r, peakmin)
        peaks[row, p]  $\leftarrow$  1
    end for
    kernel = cross_kernel(kx, ky)
    d  $\leftarrow$  dilate(peaks, idilate, kernel)
    e  $\leftarrow$  erode(d, ierode, kernel)
    contours  $\leftarrow$  find_contours(e)
    for i in 0:contours do
        if size(contours[i]) > t then
            l  $\leftarrow$  draw_contour(l, contours[i], i + 1)
        end if
    end for
    return l
end function

```

its value v and its position \mathbf{x} in space. For the probabilities conditioned on the field values (distance or diffusion field), we model the probability distributions $P(m|v, f(\mathbf{x}))$ conditioned on voxel- and field values. We want to make sure that these distribution functions vary smoothly across space (or as a function of field values), to ensure that we can identify the materials correctly across the entire image: i.e., even though the frequency distributions look completely

14 *Spatially Adapted Statistical Segmentation*

15 different close to the titanium implant compared to the middle region or sample
 16 surface, we can track the unbroken, smooth deformation to assign a global
 17 material identity.

18 To this end, we first *model the frequency distributions* using the 2D his-
 19 tograms. Given that we are modeling materials $m = 1, \dots, M$, we write the
 20 full 2D histogram as a sum of distributions $g_m(x, v)$ representing the modeled
 21 part, and a residual $r(\mathbf{x}, v)$.

$$H(x, v) = \sum_{m=1}^M g_m(x, v) + r(x, v) \quad (2)$$

22 The residual is constrained to be non-negative, i.e., we must not explain more
 23 voxels than the image contains. The distribution functions can be chosen in
 24 any way that approximately model the observed frequencies: we first used
 25 Gaussians with passable success, but found that they dropped off too rapidly.
 26 We instead found excellent results with the next-simplest model, leaving the
 27 exponential power $d_m(x)$ as a free parameter:

$$g_m(x, v) = a_m(x) e^{-b_m(x)|v - c_m(x)|^{d_m(x)}} \quad (3)$$

33 In Eq. (3), each field value x $a(x)$ is the distribution height at the center
 34 $v = c(x)$; $b(x)$ is the exponential falloff rate; and $d(x)$ is the exponential power
 35 ($d = 2$ yields a Gaussian, $d = 1$ a simple exponential). In practice we found
 36 $1.5 \leq d \leq 2$ to best match the actual frequency distribution decay rates.

37 Using the ridges found in the previous step, we generate good starting
 38 guesses and constraints for the distribution parameters a, b, c, d : For each field-
 39 value x (corresponding to a row in the 2D histogram), we initialize the starting
 40 approximation as:

$$\begin{aligned} c_m(x) &= \underset{v}{\operatorname{argmax}} \text{ with } L[x, v] = m H(x, v) && \text{Peak position} \\ a_m(x) &= H(x, c_m(x)) && \text{Peak value} \\ b_m(x) &= 3/\text{width}_m(x)^2 && \text{Decay rate} \\ d_m(x) &= 2 && \text{Exponential power} \end{aligned} \quad (4)$$

50 where we use half the distance to the center of ridge $m + 1$ as the width
 51 $\text{width}_m(x)$, using the relation that $b = 3/w^d$ yields a 5% cutoff at w for any
 52 $1 \leq d \leq 2$. This approximation already yields a good approximation. Thus,
 53 the subsequent optimization using the constrained quasi-Newton optimization
 54 method L-BFGS-B[24] converges rapidly to an excellent fit. Each 1D histogram
 55 row is first optimized independently in parallel: The resulting numerical func-
 56 tions $a_m(x), \dots, d_m(x)$ are then converted into piecewise cubic functions using
 57 a least squares-based algorithm that ensures continuity and differentiability
 58 across the piecewise segments. This lets us interpolate across outliers due to
 59 noise, but equally important: extrapolate our models smoothly into the regions
 60 to noise, but equally important: extrapolate our models smoothly into the regions
 61 to noise, but equally important: extrapolate our models smoothly into the regions
 62 to noise, but equally important: extrapolate our models smoothly into the regions
 63 to noise, but equally important: extrapolate our models smoothly into the regions
 64 to noise, but equally important: extrapolate our models smoothly into the regions
 65 to noise, but equally important: extrapolate our models smoothly into the regions

16 very close to the implant, where we don't have enough voxels to produce good
 17 statistics.

18 We finally obtain the *conditional probabilities* from the material frequency
 19 distribution models g_m as:

$$20 \quad P(m|v, f(\mathbf{x})) = \frac{g_m(v, f(\mathbf{x}))}{H(v, f(\mathbf{x}))} \quad (5)$$

21
22 (well-defined where $H(v, x) > 0$, zero outside this region as $0 \leq g_m \leq H$).
 23

24 Step 5: Perform segmentation

25 The final step of the segmentation process is to apply these probabilities for
 26 segmentation. For each voxel, we obtain its voxel value and field value, which
 27 are then used to lookup in the probability distributions, giving us a probability
 28 that the voxel belongs to a certain class. The voxel is then assigned the class
 29 with the highest probability, meaning we have effectively classified the voxel
 30 based of its voxel intensity and spatial position. In addition, the segmentation
 31 confidence is quantified by the probability.
 32

33 34 **Algorithm 4** Final segmentation from the probability distributions.

```
35   function SEGMENT(voxels[nz, ny, nx], p[nclasses, fbins, vbins],  

  36     vbins, vmin, vmax, fbins, fmin, fmax)  

  37     for z, y, x in 0:nz, 0:ny, 0:nx do  

  38       v  $\leftarrow$  voxels[z, y, x]  

  39       if vmin  $\leq$  v  $\leq$  vmax then  

  40         f  $\leftarrow$  voxels[z, y, x]  

  41         if fmin  $\leq$  f  $\leq$  fmax then  

  42           vi  $\leftarrow$  (vbins - 1) -  $\frac{v - v_{\min}}{v_{\max} - v_{\min}}$   

  43           fi  $\leftarrow$  (fbins - 1) -  $\frac{f - f_{\min}}{f_{\max} - f_{\min}}$   

  44           probabilities  $\leftarrow$  p[:, fi, vi]  

  45           result[z, y, x]  $\leftarrow$  argmax(probabilities) + 1  

  46         end if  

  47       end if  

  48     end if  

  49   end for  

  50   return result  

  51 end function
```

52 53 54 55 56 4.6 Results of the field-segmentation

57 Here we present the final output from the steps described above.
 58
 59
 60
 61
 62
 63
 64
 65

16 *Spatially Adapted Statistical Segmentation***4.6.1 Sub-classification of soft tissue**

With a good separation of soft tissue and bone, we map out the blood vessel network using connected components analysis, which is visualized in the 3D renders in [Figure 10](#). Here we see that we have successfully segmented the blood vessels out of the bone region. It is especially prominent when looking at the capillary network, as we can see these in fine detail. Noteworthy, the newly formed bone region ([Figure 10b](#)) contains a larger concentrations of these small blood vessels, compared to the old bone ([Figure 10a](#)). If we zoom in to a small cube region ([Figure 10c](#) and [Figure 10d](#)), we see it even more defined, clearly seeing how the larger vessels connect through the smaller ones.

The osteocytes are selected by volume and shape: For every connected component in the feasible volume range, its principal axis and best ellipsoid is computed and checked against the potential osteocyte shape.

4.7 Assessing bone-implant contact and blood-implant contact

Once segmented, tissue in contact with the implant can be studied using the Euclidean Distance Transform (EDT) from the implant, restricted to the bone region. We can simply mask the voxels that are within a thin shell of distances, $d_{min} < d(x, y, z) \leq d_{max}$, for example $d_{min} = 1\mu m$ to $d_{max} = 5\mu m$. We then sum over the masked voxels of each tissue type to obtain and divide by the total to obtain the tissue-to-implant contact per area, or study the distribution across the surface area qualitatively.

A larger quantitative study is planned that analyses the full data set against recently conducted histological microscopy taken from the same biopsies. In the present work, we evaluate qualitatively: Since the SR μ CT tomograms are clear enough that it is possible as humans to distinguish between blood vessels and bone, as our mammalian visual cortex automatically corrects for the distortion effects, we can verify the success of the automatic classification.

Figures [11](#) and [12](#) show the same 2D slices as were shown in Figures [1](#) and [2](#), allowing us to visually inspect them side by side. The voxels are coloured according to the segmentation confidence, with degree of red proportional to the modeled probability $P(0|v, x)$ and degree of yellow proportional to $P(1|v, x)$. Grey voxels indicate low model probabilities of both: either due to the voxel belonging to another material, or simply low computed confidence of the model. By comparing against Figures [11](#) and [12](#), we see that the computed classification matches the human classification everywhere where it is possible to visually distinguish the voxels. However, in a thin 1-voxel border to the implant, we cannot verify the segmentation, as the voxel values are so blended together with the implant voxel values that they become indistinguishable. A further strengthening of the analysis is needed in order to reach this layer. It is possible that the information is irretrievably lost, or perhaps it can be retrieved through a deconvolution - or simply a more precise version of the present analysis.

5 Conclusion and future work

While SR μ CT yields 3D reconstructions of extremely high fidelity compared to lab-grade X-ray setups, several distortion effects remain that obstruct accurate tissue classification in important regions, in particular near and at interfaces of high-contrast transitions such as where biological tissue meets metallic implants. However, these effects are well behaved, in the sense that they vary smoothly over space, making it possible to discover approximate mathematical models of the effects, and counter their resulting distortion.

We were able to build probabilistic models for the distortive effects of soft tissue and bone voxel values as functions of distance to the implant, and as functions of an approximate diffusion field. This made it possible to see all the way up to the implant surface, and automatically segment into tissue types throughout the sample and all the way up to the implant surface, with high accuracy both at long and short distances.

In this pilot work, we have only made a qualitative study. In upcoming work, we plan a larger quantitative study that compares with histology microscopy results, obtained from the same biopsies. In addition, we are extending the method with Bayesian combination of multiple “angles”: different sources of distortion effects (e.g. multiple physical effects) can be better captured by different fields, e.g. beam hardening may be best captured by the distance transform to the sample surface, while the diffusion field captures distortion near metallic implants. Thus different fields separate tissue material distributions in different regions, and in combination are expected to yield a stronger analysis. It is hoped that this will make it possible to separate multiple highly overlapping frequency distributions.

6 Acknowledgements

This project has received funding from the European Union’s Horizon 2020 research and innovation programme under grant agreement No. 779322 (“MAXIBONE”). JA was partially supported by the VILLUM Foundation through VILLUM Experiment Project: 41017. CJ was funded by the Innovation Fund Denmark (IFD) under File No. 8057-00012B, the IFD Grand Solutions project “Adaptive X-ray InSpection”.

7 Conflict of Interest

On behalf of all authors, the corresponding author states that there is no conflict of interest.

References

- [1] Lauridsen, T., Feidenhans'l, R., Pinholt, E.M.: Virtual histology uncertainty in synchrotron x-ray micro-computed tomography evaluation. Journal of Cranio-Maxillo-Facial Surgery **46**, 1569–1574 (2018)

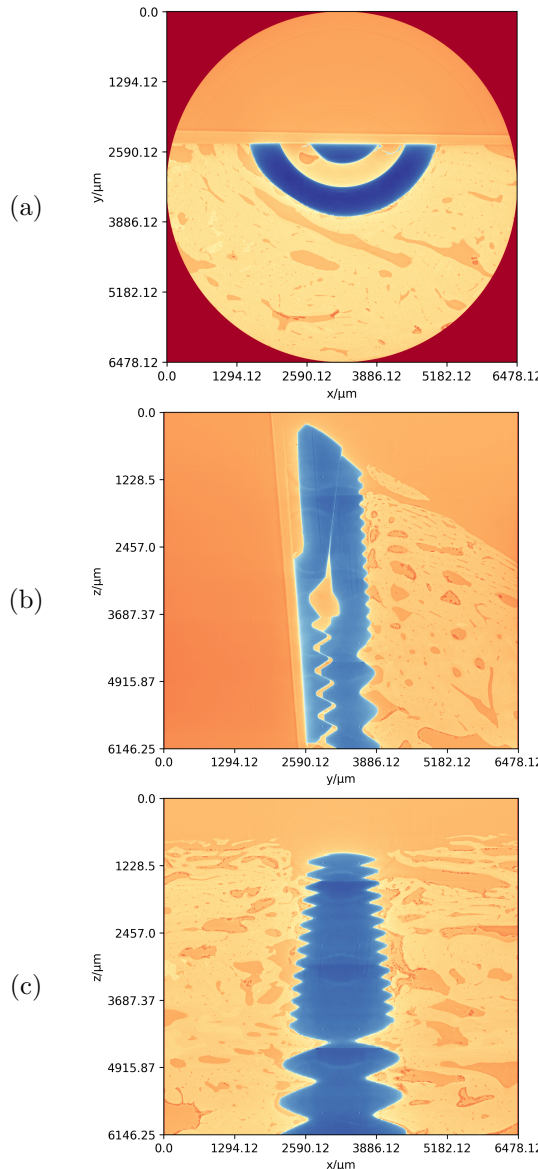
18 *Spatially Adapted Statistical Segmentation*

- [2] Neldam, C.A., Sporring, J., Rack, A., Lauridsen, T., Hauge, E.-M., Jørgensen, H.L., Jørgensen, N.R., Feidenhansl, R., Pinholt, E.M.: Synchrotron radiation μ ct and histology evaluation of bone-to-implant contact. *Journal of Cranio-Maxillo-Facial Surgery* **45**(9), 1448–1457 (2017)
- [3] Frost, H.: The biology of fracture healing. an overview for clinicians. part i. *Clinical orthopaedics and related research* (248), 283–293 (1989)
- [4] Berglundh, T., Abrahamsson, I., Lang, N.P., Lindhe, J.: De novo alveolar bone formation adjacent to endosseous implants. *Clinical Oral Implants Research* **14**(3), 251–262 (2003). <https://doi.org/10.1034/j.1600-0501.2003.00972.x>
- [5] Abrahamsson, I., Berglundh, T., Linder, E., Lang, N.P., Lindhe, J.: Early bone formation adjacent to rough and turned endosseous implant surfaces. an experimental study in the dog. *Clinical Oral Implants Research* **15**(4), 381–392 (2004). <https://doi.org/10.1111/j.1600-0501.2004.01082.x>
- [6] Franchi, M., Orsini, E., Triré, A., Quaranta, M., Martini, D., Piccari, G.G., Ruggeri, A., Ottani, V.: Osteogenesis and morphology of the peri-implant bone facing dental implants. *The Scientific World JOURNAL* **4**, 1083–1095 (2004). <https://doi.org/10.1100/tsw.2004.211>
- [7] Neldam, C.A., Lauridsen, T., Rack, A., Lefolii, T.T., Jørgensen, N.R., Feidenhans'l, R., Pinholt, E.M.: Application of high resolution synchrotron micro-ct radiation in dental implant osseointegration. *Journal of Cranio-Maxillofacial Surgery* **43**(5), 682–687 (2015). <https://doi.org/10.1016/j.jcms.2015.03.012>
- [8] Erben, R.G.: Embedding of bone samples in methylmethacrylate: an improved method suitable for bone histomorphometry, histochemistry, and immunohistochemistry. *Journal of Histochemistry & Cytochemistry* **45**(2), 307–313 (1997)
- [9] Ferguson, S., Bryant, J., Ito, K.: Three-dimensional computational reconstruction of mixed anatomical tissues following histological preparation. *Medical engineering & physics* **21**(2), 111–117 (1999)
- [10] Eugene Lin, A.A.: What are the basic concepts of temporal, contrast, and spatial resolution in cardiac ct? *Journal of Cardiovascular Computed Tomography* **3**, 403–408 (2009). <https://doi.org/10.1016/j.jcct.2009.07.003>
- [11] Rack, A., Stroebel, J., Rack, T., Dabin, Y., Knabe, C., Stiller, M., Coan, P., Bleuet, P.: Tomopress-in situ synchrotron-based microtomography under axial load. *Instruments* **4**, 11 (2020). <https://doi.org/10.3390/instruments4020011>

- 15 [12] Vidal, F.P., Létang, J.M., Peix, G., Cloetens, P.: Investigation of arte-
16 fact sources in synchrotron microtomography via virtual x-ray imaging.
17 Nuclear Instruments and Methods in Physics Research B **234**, 333–348
(2005). <https://doi.org/10.1016/j.nimb.2005.02.003>
- 18 [13] Mirone, A., Brun, E., Gouillart, E., Tafforeau, P., Kieffer, J.: The pybst2
19 hybrid distributed code for high speed tomographic reconstruction with
20 iterative reconstruction and a priori knowledge capabilities. Nuclear
21 Instruments and Methods in Physics Research Section B: Beam Interac-
22 tions with Materials and Atoms **324**, 41–48 (2014). <https://doi.org/10.1016/j.nimb.2013.09.030>. 1st International Conference on Tomography of
23 Materials and Structures
- 24 [14] Mirone, A., Brun, E., Gouillart, E., Tafforeau, P., Kieffer, J.: The pybst2
25 hybrid distributed code for high speed tomographic reconstruction with
26 iterative reconstruction and a priori knowledge capabilities. Nuclear
27 Instruments and Methods in Physics Research Section B: Beam Interac-
28 tions with Materials and Atoms **324**, 41–48 (2014). <https://doi.org/10.1016/j.nimb.2013.09.030>. 1st International Conference on Tomography of
29 Materials and Structures
- 30 [15] Ketcham, R.A., Hanna, R.D.: Beam hardening correction for x-ray com-
31 puted tomography of heterogeneous natural materials. Computers &
32 Geosciences **67**, 49–61 (2014). <https://doi.org/10.1016/j.cageo.2014.03.003>
- 33 [16] Bolstad, K., Flatabø, S., Aadnevik, D., Dalehaug, I., Vetti, N.: Metal arti-
34 fact reduction in ct, a phantom study: subjective and objective evaluation
35 of four commercial metal artifact reduction algorithms when used on three
36 different orthopedic metal implants. Acta Radiologica **59**(9), 1110–1118
37 (2018). <https://doi.org/10.1177/0284185117751278>. PMID: 29310445
- 38 [17] Huang, V., Kohli, K.: Su-e-i-13: Evaluation of metal artifact reduction
39 (mar) software on computed tomography (ct) images. Medical Physics
40 **42**(6Part5), 3244–3244 (2015). <https://doi.org/10.1118/1.4924010>
- 41 [18] Cloetens, P., Ludwig, W., Baruchel, J., Van Dyck, D., Van Landuyt,
42 J., Guigay, J.P., Schlenker, M.: Holotomography: Quantitative phase
43 tomography with micrometer resolution using hard synchrotron radia-
44 tion x rays. Applied Physics Letters **75**(19), 2912–2914 (1999). <https://doi.org/10.1063/1.125225>
- 45 [19] Cloetens, P., Ludwig, W., Boller, E., Helfen, L., Salvo, L., Mache, R.,
46 Schlenker, M.: Quantitative phase contrast tomography using coherent
47 synchrotron radiation. International Society for Optics and Photonics
48 **4503**, 82–91 (2002). <https://doi.org/10.1117/12.452867>

20 *Spatially Adapted Statistical Segmentation*

- [20] Croton, L.C.P., Ruben, G., Morgan, K.S., Paganin, D.M., Kitchen, M.J.: Ring artifact suppression in x-ray computed tomography using a simple, pixel-wise response correction. Opt. Express **27**(10), 14231–14245 (2019). <https://doi.org/10.1364/OE.27.014231>
- [21] Boas, F., Fleischmann, D.: Ct artifacts: Causes and reduction techniques. Imaging in Medicine **4** (2012). <https://doi.org/10.2217/iim.12.13>
- [22] Cong, W., Wang, G.: X-ray scattering tomography for biological applications. Journal of X-ray science and technology **19**, 219–27 (2011). <https://doi.org/10.3233/XST-2011-0288>
- [23] Lab, S.: GitHub page for seung-lab/euclidean-distance-transform-3d: Euclidean distance & signed distance transform for multi-label 3D anisotropic images using marching parabolae. <https://github.com/seung-lab/euclidean-distance-transform-3d/> ([Accessed online: 28th June 2022])
- [24] Zhu, C., Byrd, R.H., Nocedal., J.: L-bfgs-b: Algorithm 778: L-bfgs-b, fortran routines for large scale bound constrained optimization. ACM Transactions on Mathematical Software **23**(4), 550–560 (1997)



56 **Fig. 1:** Cut sample seen as cross sections in XY, YZ and XZ-planes respectively.
57 A voxel has a size of $1.875\mu\text{m}$. Red voxels are numerically low, while
58 blue voxels are high.

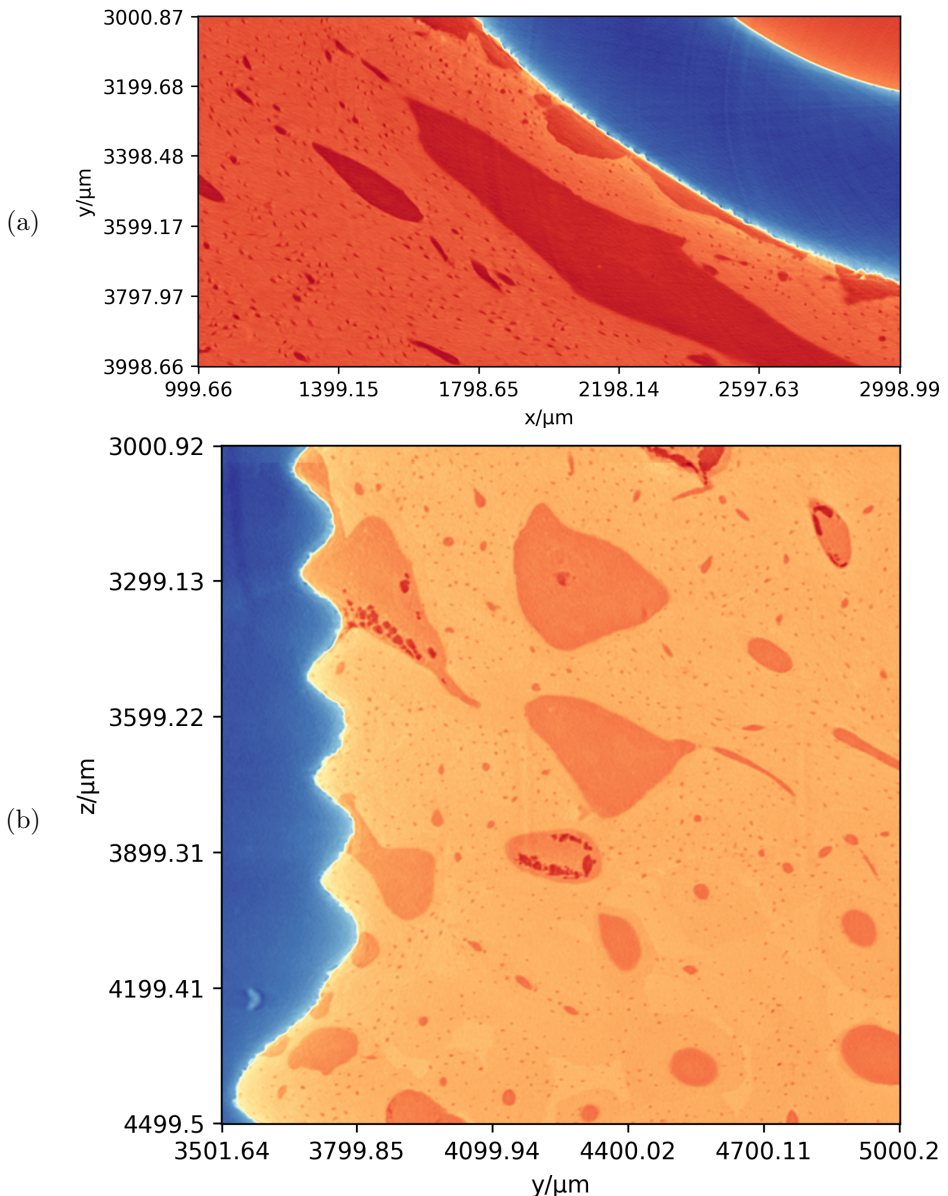
22 *Spatially Adapted Statistical Segmentation*

Fig. 2: To better see the distortion effects, we zoom in on sub-regions of the slices shown in Figure 1. Our visual systems automatically correct for most of the distortions, as they appear similar to illumination effects. However, even some distance from the implant, blood vessel voxels have higher values than bone voxels further out. As we approach the implant, the value-shifts accelerates and becomes highly non-linear. (a) A $1\text{mm} \times 2\text{mm}$ region of an image slice in the XY-plane. (b) A $1.5\text{mm} \times 1.5\text{mm}$ region of an image slice in the YZ-plane in the micro threaded part of the titanium implant.

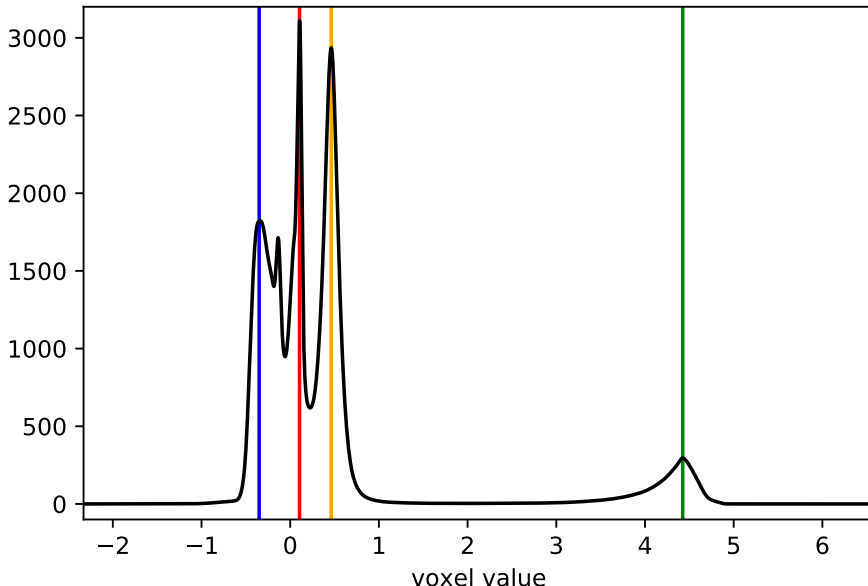


Fig. 3: 1-dimensional histogram of the voxel values of a tomography. The blue line is air peak, the red line is the soft tissue peak, the green line is the bone peak, and the orange line is the implant peak.

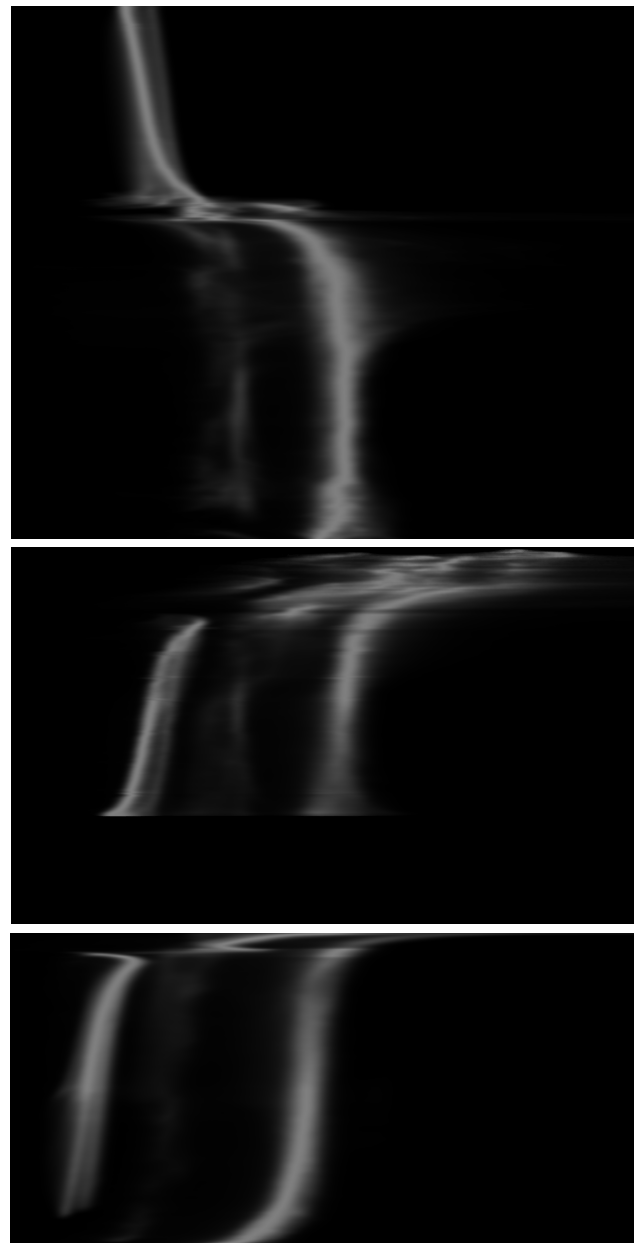
10
11
12
13
14
15
16
17
18
19
20
21
22
23
24
25
26
27
28
29
30
31
32
33
34
35
36
37
38
39
40
41
42
43
44
45
46
47
48
49
50
51
52
53
54
55
56
57
58
59
60
61
62
63
64
6524 *Spatially Adapted Statistical Segmentation*

Fig. 4: Examples of 2D histograms for the full tomogram: (a) along the y -axis, (b) as a function of distance r to the center, and (c) as a function of distance d to the implant. The abscissa of the 2D histograms is voxel value, the ordinate is the value of y resp. r and d . Notice that the r -2D histogram well separates the materials for large and intermediate values of r , but breaks down for small r . However, it clearly shows a brightening trend for small r .

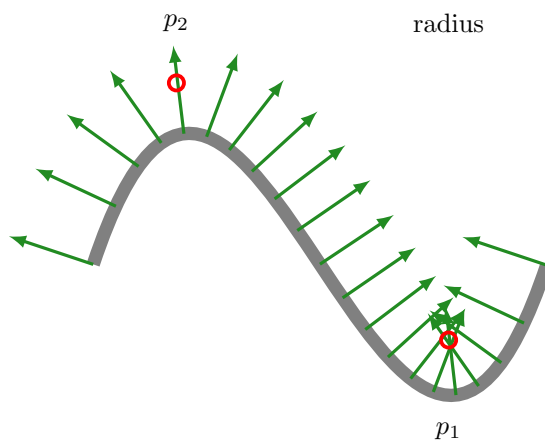


Fig. 5: Visualization of glowing effect close to the implant surface, shown in the YZ plane. The two points p_1 and p_2 , marked in red, have the same distance to the implant, but receive markedly different brightening effect. Diffusion is depicted in green, where we see multiple arrows contributing to the value of p_1 . The dotted line depicts a constant radius from the tomogram center.

26 *Spatially Adapted Statistical Segmentation*51 **Fig. 6:** A slice of the diffusion field in the YZ plane.
52
53
54
55
56
57
58
59
60
61
62
63
64
65

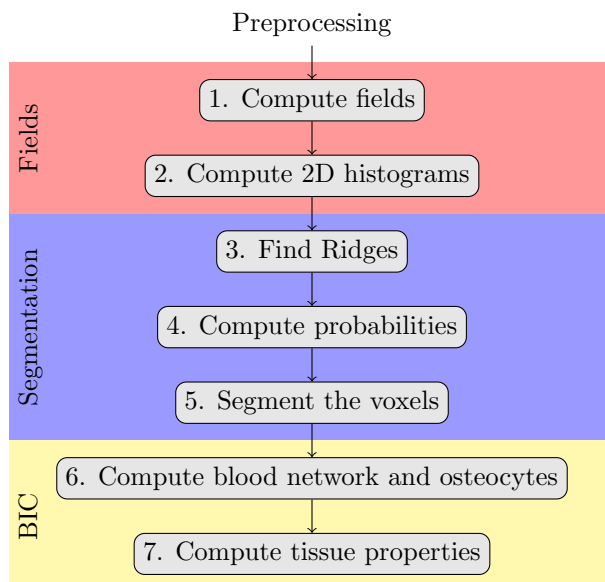
10
11
12
13
14
15
16
17
18
19
20
21
22
23
24
25
26
27
28
29
30
31
32
33
34
35
36
37
38
39
40
41
42
43
44
45
46
47
48
49
50
51
52
53
54
55
56
57
58
59
60
61
62
63
64
65

Fig. 7: Flowchart depicting the steps of the method.

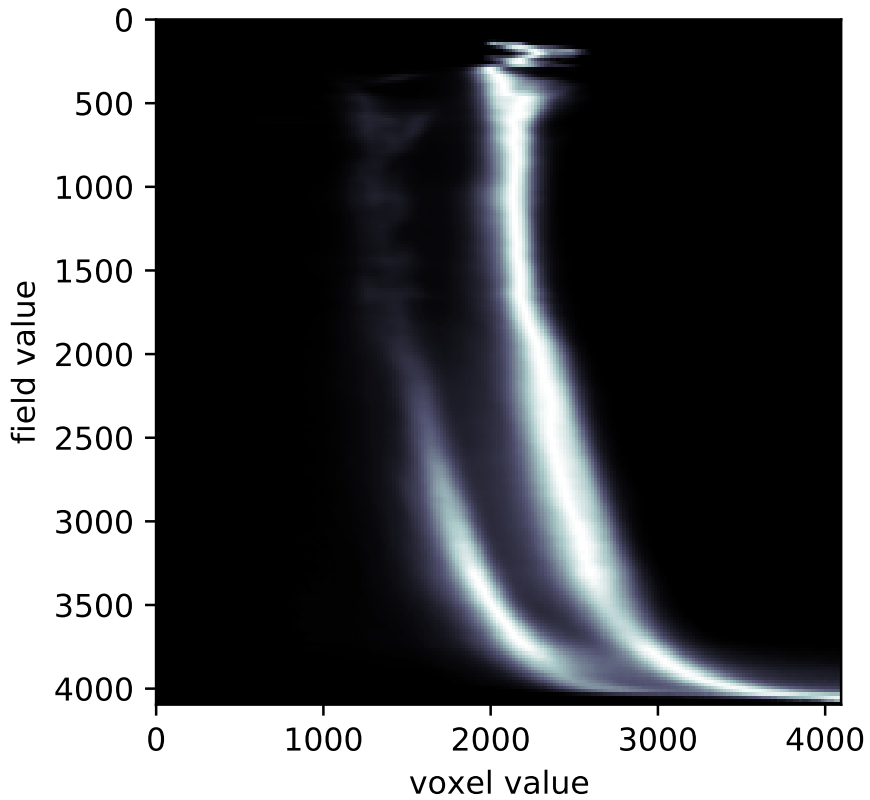


Fig. 8: 2D field histogram. Note that there are two clearly separated ridges, which each represent the expectation value for a particular material as a function of the field value.

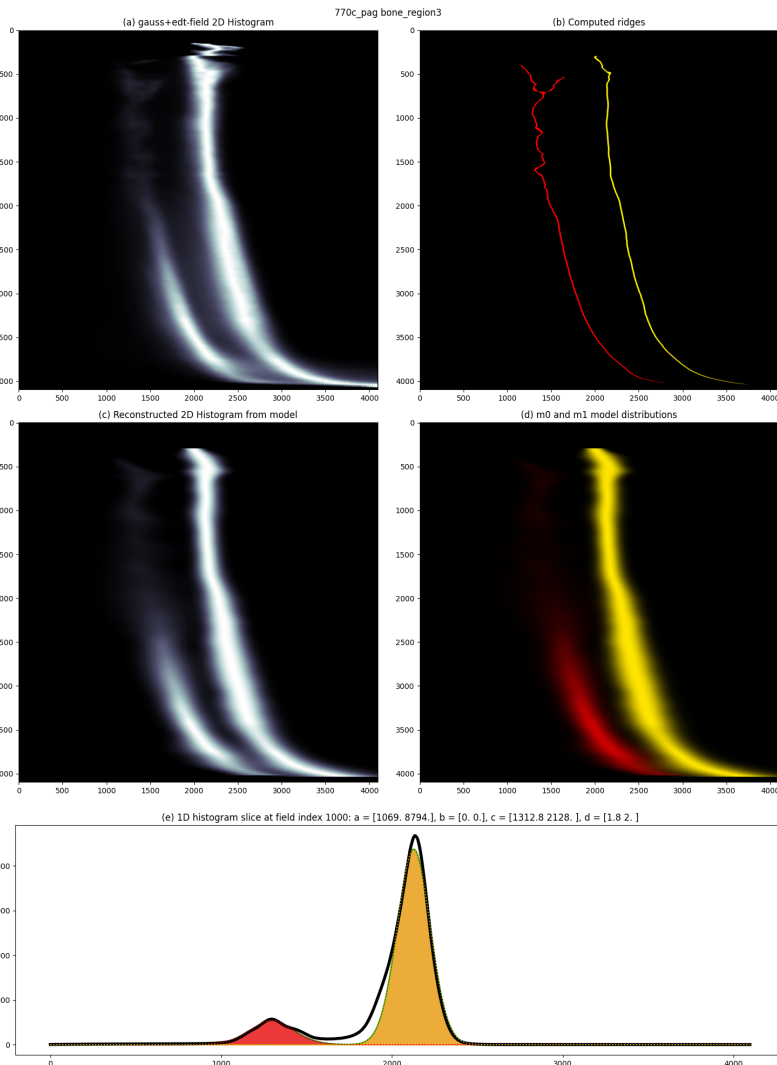
10
11
12
13
14
15

Fig. 9: (a) Measured 2D histogram for the compound diffusion+distance field from Step 2. (b) The detected ridges from Step 3. (c) Sum of computed frequency distribution models with optimized smooth piecewise cubic functions for parameters $a(x), b(x), c(x), d(x)$: this is the part of the 2D histogram explained by the smooth model. (d) The individual distributions evaluated on the 2D field-value \times voxel-value grid. (e) A single 1D slice of the 2D histogram (black) together with the model frequency distributions. Red is soft-tissue, yellow is bone mineral.

60
61
62
63
64
65

30 *Spatially Adapted Statistical Segmentation*
27
28
29
30
31
32
33
34
35
36
37
38
39
40
41
42
43
44
45
46
47
48
49
50
51
52
53
54
55
56
57
58
59
60
61
62
63
64
65(a) A $375\mu m \times 4230\mu m \times 6480\mu m$ slice of the blood network in the old bone region.
27
28
29
30
31
32
33
34
35
36
37
38
39
40
41
42
43
44
45
46
47
48
49
50
51
52
53
54
55
56
57
58
59
60
61
62
63
64
65(b) A $375\mu m \times 4230\mu m \times 6480\mu m$ slice of the blood network in the new bone region.
27
28
29
30
31
32
33
34
35
36
37
38
39
40
41
42
43
44
45
46
47
48
49
50
51
52
53
54
55
56
57
58
59
60
61
62
63
64
65(c) A $1mm \times 1mm \times 1mm$ cube of the blood network in the old bone region. (d) A $1mm \times 1mm \times 1mm$ cube of the blood network in the new bone region.
27
28
29
30
31
32
33
34
35
36
37
38
39
40
41
42
43
44
45
46
47
48
49
50
51
52
53
54
55
56
57
58
59
60
61
62
63
64
65

Fig. 10: 3D renders of the blood network. Note the difference between the the capillary network in the old bone region (10a,10c) compared to the newly grown bone region (10b,10d).

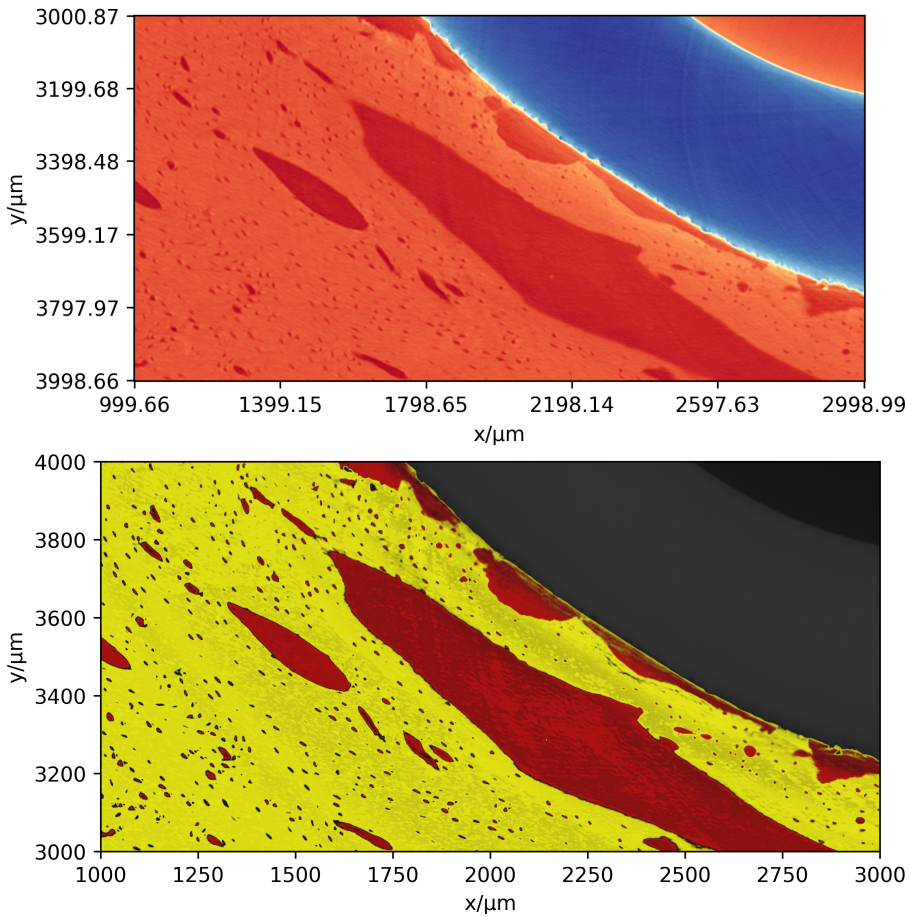


Fig. 11: XY slices of the original tomography (top), and the classified (bottom). The voxels are coloured according to the modeled probability functions $P(m|v, x)$ between 0 and 1: completely red voxels have $P(m = 0|v, x) = 1$, completely yellow voxels have $P(m = 1|v, x) = 1$, and uncertain voxels become progressively gray.

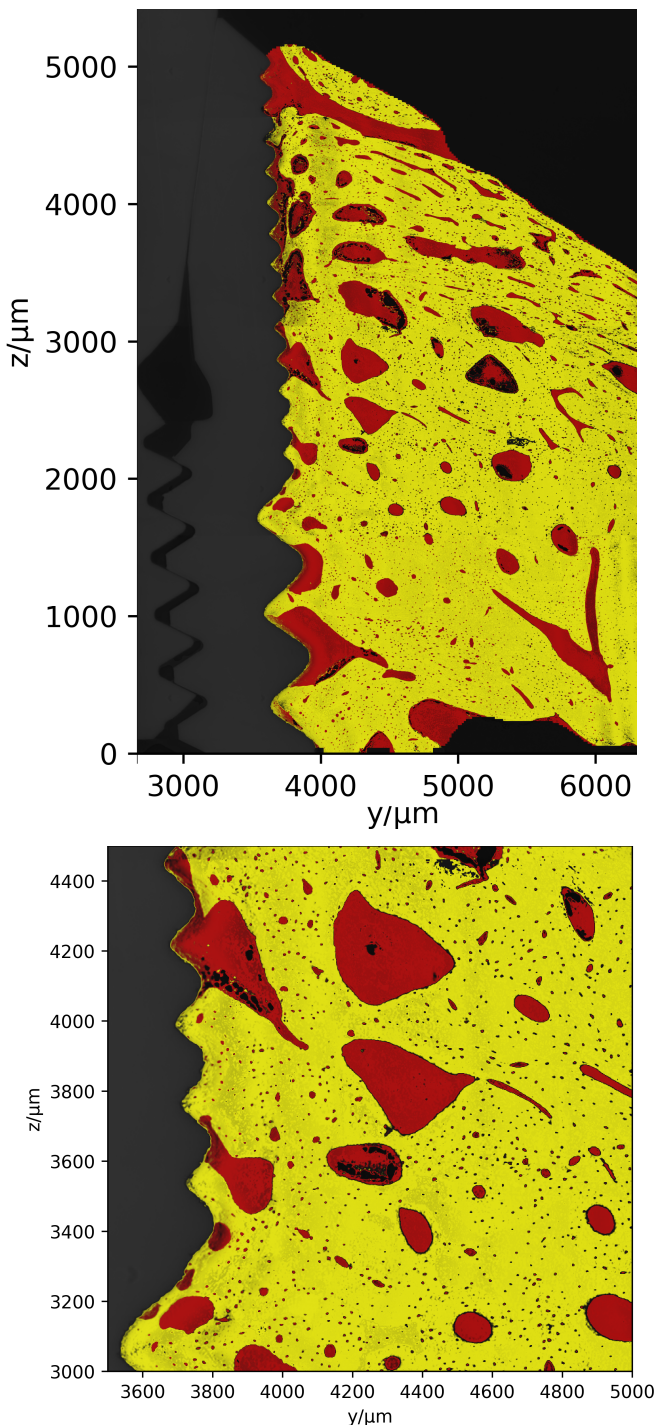
32 *Spatially Adapted Statistical Segmentation*

Fig. 12: ZY slices of the segmentation seen far away (top) and zoomed in (bottom). Yellow depicts bone and red depicts soft-tissue. Note that the segmentation correctly classifies the materials close to the implant, even in the grooves of the screw threads..